https://doi.org/10.5194/egusphere-2025-6300
Preprint. Discussion started: 6 March 2026

Ice dynamics in McMurdo Sound, Antarctica, based on precise synthetic aperture radar interferometry analysis

Kallie Bohn[1], Wolfgang Rack[1], Daniel Price[1], Mathieu Sellier[2], and Rodrigo Gomez-Fell[3]

[1]Gateway Antarctica, School of Earth and Environment, University of Canterbury, Private Bag 4800, Ōtautahi | Christchurch, Aotearoa | New Zealand
[2]Mechanical Engineering, University of Canterbury, Private Bag 4800, Ōtautahi | Christchurch, Aotearoa | New Zealand
[3]Waterways Centre for Freshwater Management, School of Earth and Environment, University of Canterbury, Private Bag 4800, Ōtautahi | Christchurch, Aotearoa | New Zealand

Correspondence: Kallie Bohn (kal.bohn@pg.canterbury.ac.nz)

https://doi.org/10.5194/egusphere-2025-6300
Preprint. Discussion started: 6 March 2026

Abstract. The embayment at the end of Ross Island's Hut Point Peninsula is often covered by a patch of landfast sea ice (henceforth *fast ice*), which can remain attached to the McMurdo Ice Shelf (MIS) for a few years at a time, rather than breaking out every summer. Over recent years, later fast ice formation and increased fast ice breakout have been observed, but the influence on ice shelf stability is unclear. We examined historical MIS front positions, as well as the summer 2025 fast ice breakout and MIS calving, using Landsat optical imagery and historical USGS aerial photography.

A precise interferometric satellite analysis was conducted for spring 2024 based on ascending-descending combinations of TerraSAR-X image acquisitions. Two non-orthogonal horizontal component velocity fields were calculated, and ground-referenced with precise movement data acquired with three automated GNSS stations that had been placed on the ice. This allowed us to calibrate three simply connected subsets to each of the velocity field components: the MIS itself, the multi-year fast ice, and the first-year fast ice. These component fields then enabled us to calculate a near-complete 2D horizontal velocity field of ice motion in the area. This analysis was the basis for calculating the divergence field of the velocity as well as principal strain rate fields. The overall ice dynamics were then related to the areas where we expect a stabilizing effect of the fast ice on the ice shelf front, or where the ice shelf geometry suggests stabilizing effects.

Once the January–February 2025 fast ice breakout was complete, the MIS front began calving almost immediately, leading to a net retreat of the MIS front to a minimum beyond any other found in the Landsat 4–9 record. The dynamics of the fast ice were largely dependent on age, with the behavior of the multi-year fast ice resembling in most ways that of the adjoining MIS rather than the first-year fast ice, due to strong coupling at the MIS–multi-year fast ice interface. The divergence of the velocity field and the principal strain rates show convergence and compression of the fast ice in the embayment, providing evidence of a stabilizing effect and possible buttressing of the MIS by fast ice.

Plain-Language Summary

As *ice sheets* – the vast masses of ice that cover the continent of Antarctica – slowly flow into the ocean, they form floating *ice shelves*. These ice shelves obstruct and slow the flow of glaciers and ice sheets into the ocean, and so the stability of ice shelves is of crucial concern for understanding the future of Antarctica's ice sheets. Meanwhile, *landfast sea ice* – the ice that forms from frozen seawater and is fastened to land and to the edges of ice shelves – helps to preserve ice shelves: it can prevent the calving of icebergs by physically holding the edges of ice shelves together, and protects them from ocean swells. Thus, better understanding these interactions between landfast ice and ice shelves can help us understand the behavior and fate of ice sheets.

The McMurdo Ice Shelf (MIS), in particular, is also important to the infrastructure that supports the many and varied scientific operations in McMurdo Sound. The Antarctic stations in McMurdo Sound – Scott Base and McMurdo Station – rely on personnel and supplies that often arrive by aircraft that land on the MIS, which then travel to their destination via a road that is also on the ice shelf. Better understanding the role of landfast ice in stabilizing the MIS is valuable for the future of these operations.

https://doi.org/10.5194/egusphere-2025-6300
Preprint. Discussion started: 6 March 2026

For most of each year, the sometimes-open water of McMurdo Sound is covered by landfast ice. Every summer, most of the landfast ice breaks apart and floats out to sea. However, near Hut Point Peninsula, patches of landfast ice often remain intact and attached to the MIS for several years. We studied the conditions before the summer 2025 landfast ice breakout, during which multi-year landfast ice broke apart, exposing a portion of the MIS to open water for the first time in nearly three years. Less than a day later, icebergs began breaking off from the MIS.

We used a radar satellite–based technique that allowed us to use a pair of images looking at the same area, from the same direction, at different times, to calculate how much the ice moved toward or away from the direction the satellite was looking, in the 11 days between images. We did this with two pairs of images looking from different directions, which let us calculate the true movement of the ice during an 11-day period in early November of 2024. Using data from three positional sensors we had placed on the ice in the spring, we could adjust the movement we calculated to make sure it matched what our sensors measured. Once we knew how the ice had been moving, we could calculate where it was being forced into a smaller area or expanding into a larger one.

Our results told us about how the MIS, multi-year landfast ice, and first-year landfast ice behave and interact. As the MIS pushed into the multi-year landfast ice, the multi-year ice absorbed some of the force, being compressed in the process and losing a little speed as it was pushed forward. Where the multi-year and first-year ice attached to each other, the multi-year ice passed along some of the force applied to it by the MIS. As the first-year ice absorbed this force, it compressed more and quickly lost more speed than the multi-year ice did.

These connections go both ways: the first-year landfast ice pushes back against the multi-year landfast ice, which pushes back against the MIS. But since the edge of the MIS was not deforming in response, we conclude that the multi-year ice pushing into it must have been stabilizing it instead of changing it. The suddenness, speed, and amount of icebergs that broke off of the MIS once the multi-year ice was gone, suggest that this stabilizing effect is strong, and our calculations further indicate its importance in preserving the MIS. If future landfast ice breaks apart earlier, our findings suggest more icebergs breaking off of the MIS should be expected, potentially threatening the stability of the MIS. As the Antarctic ice changes in response to warming air and water, it will be important to better understand this stabilizing effect, in order to also better understand the future of the McMurdo Ice Shelf and the East Antarctic Ice Sheet.

1 Introduction

Better understanding the dynamical interactions between landfast sea ice (henceforth *fast ice*) and ice shelves – and the timing of fast ice breakout and ice shelf calving events – may provide insights into the future behavior and possible retreat of the McMurdo Ice Shelf (MIS). One tool for such investigation is Interferometric Synthetic Aperture Radar (InSAR), which allows us to calculate surface displacement with high precision. The applications of InSAR for studying fast ice are numerous. It has been used to map fast ice extent (e.g. Meyer et al., 2011; Wang et al., 2021), detect its surface displacement (e.g. Morris et al., 1999; Van der Sanden and Short, 2017), evaluate its surface roughness and topography (e.g. Dammann et al., 2017; Dierking et al., 2017), investigate the stability, deformation, and fracturing of fast ice (e.g. Chen et al., 2021; Dammann et al.,

https://doi.org/10.5194/egusphere-2025-6300
Preprint. Discussion started: 6 March 2026

2016, 2018, 2019; Li et al., 1996), study infragravity waves and tidal strain in sea ice (e.g. Han and Lee, 2018; Mahoney et al., 2016), analyze fast ice breakout patterns (e.g. Jensen et al., 2023), and calculate thermal and dynamical strain in fast ice (e.g. Fedders et al., 2024).

For McMurdo Sound, Gomez-Fell et al. (2024) used InSAR to investigate the stabilizing effect of fast ice on the Erebus Ice Tongue. We used a similar approach, focusing farther south, on the combined fast ice–MIS system, during the transition between winter and summer 2024–2025, in order to examine the dynamics of the system with the goal of better understanding the behavior and stability of the MIS.

While ice shelves have a buttressing effect on the glaciers and ice sheets they extend from (Dupont and Alley, 2005; Rott et al., 2017; Wuite et al., 2015), fast ice helps to preserve ice shelves and glacier tongues by adding inertia to the system. This inertia plays a role in physically stabilizing calving fronts, while providing some protection from ocean swells (Christie et al., 2022; Gomez-Fell et al., 2022; Massom et al., 2018; Miles et al., 2017). Improving our understanding of the interactions between fast ice and grounded ice thus improves our understanding of ice sheet evolution and stability.

Additionally, the MIS is the location of the airfields that are crucial for the logistics of the Ross Island stations, deep field operations, and the South Pole Station, as well as for aircraft-based scientific operations (e.g. Haas et al. (2021); Rack et al. (2021); Tinto et al. (2019)).

2 Study Area

McMurdo Sound (Fig. 1) is a region with complex interactions between ice shelf, sea ice, and ocean (Gow and Govoni, 1994; Leonard et al., 2011, 2021; Mahoney et al., 2011; Price et al., 2014; Richter et al., 2024; Robinson et al., 2010; Smith et al., 2001). During most of the year, the MIS is bounded by fast ice that covers the Sound (Fraser et al., 2012; Lanhorne et al, 2023). Most of this fast ice undergoes a yearly summer breakout (Kim et al., 2018). However, in the embayment near the end of Hut Point Peninsula, patches of fast ice often remain intact and attached to the MIS edge for a few years at a time.

Since the 1960s, the MIS front in the embayment has at times undergone retreat and advancement (Fig. 1). From 1963 to 1989, large net retreat occurred, followed by more net retreat between 1989 and 1999, and net advance from 1999 to 2004. Between 2004 and 2014, part of the MIS front underwent net advance, and part net retreat. Further net retreat occurred between 2014 and 2025. The amount of calving and net retreat may be related to changes in the formation and duration of fast ice.

In January and early February of 2025, the annual fast ice breakout occurred in McMurdo Sound. In addition to the breaking-up and floating-away of the seasonal first-year fast ice, at the end of Ross Island's Hut Point Peninsula, a patch of multi-year-old fast ice broke apart. By 30 January, almost all of the first-year fast ice had broken out, but almost all of the multi-year fast ice remained. Following several days of strong winds, the next clear Landsat image showed that the fast ice breakout was complete by 02 February. This exposed a portion of the MIS to open water for the first time in nearly three years. Less than a day after the fast ice breakout was complete, the MIS began calving icebergs. Figure 2 shows the progression of the breakout and calving in summer 2025.

https://doi.org/10.5194/egusphere-2025-6300
Preprint. Discussion started: 6 March 2026

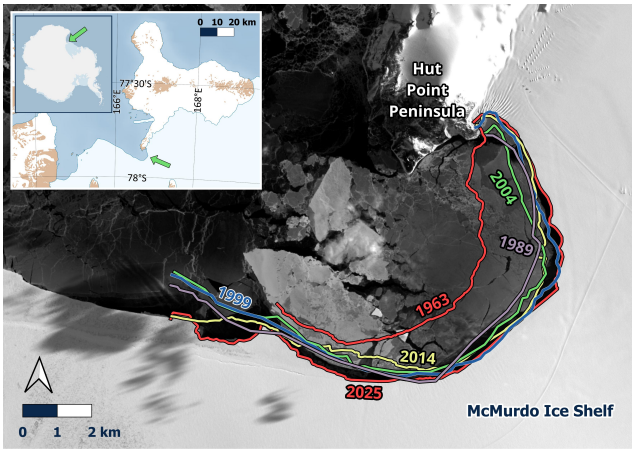

Figure 1. MIS extent near Hut Point. 1963 line traced from USGS aerial photography image obtained via the Polar Geospatial Center; 1989–2025 lines traced from Landsat imagery (EROS, 2020a, b, c). (Background: Landsat panchromatic band, 13 March 2025 (EROS, 2020c). Insets made using Quantarctica (Matsuoka et al., 2018) and datasets included therein (Amante and Eakins, 2009; Arndt et al., 2013; Liu et al., 2015; data from the SCAR Antarctic Digital Database, 2013).)

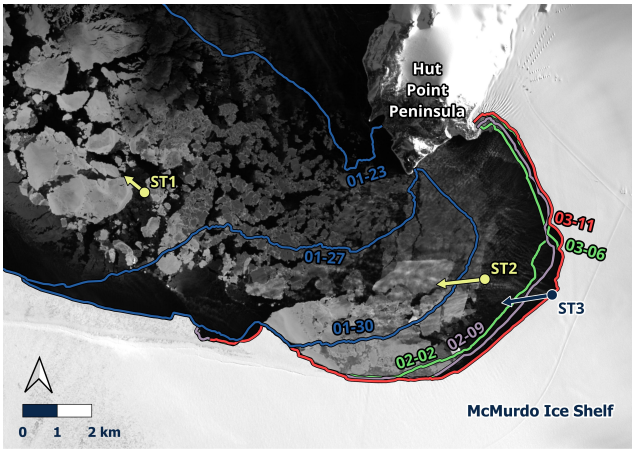

Figure 2. Ice extent near Hut Point during summer 2025 fast ice breakout and MIS calving. Blue lines: ice extend during fast ice breakout; other colors: MIS front position after breakout. Arrows indicate average horizontal station motion from 29 October 2024 to 28 November 2024: 9.383 cm d^{-1} for Station 1; 26.925 cm d^{-1} for Station 2; 28.586 cm d^{-1} for Station 3. (Background: Landsat panchromatic band, 12 March 2025 (EROS, 2020c).)

3 Data and Methods

We used GNSS and InSAR data to characterize the ice dynamics in McMurdo Sound during the 2024/2025 spring and summer.
100 In October of 2024 three automated GNSS stations where placed in the vicinity of Hut Point Peninsula on the first-year fast ice,

https://doi.org/10.5194/egusphere-2025-6300
Preprint. Discussion started: 6 March 2026

multi-year fast ice, and the MIS near its edge. The stations remained deployed until the following November, December, and February, respectively. The GNSS data were used in combination with Synthetic Aperture Radar imagery from the TerraSAR-X mission to calculate precise 2-dimensional horizontal vector field displacements, ice divergence, and principal strain rates.

GNSS data processing was conducted using Trimble Business Center. InSAR processing was performed using Gamma Remote Sensing.

3.1 Automated GNSS stations

On 21 October 2024, three automated GNSS stations were placed on the ice near Hut Point Peninsula: one on the first-year fast ice (ST1), one on the multi-year fast ice (ST2), and one on the MIS near its edge (ST3)(Fig. 2). Each of these stations consists of a Trimble R9 GNSS unit and tiltmeter for tracking the position and orientation of the ice surface over time, datalogger for the tiltmeter timeseries, solar panel and battery, free-standing metal frame, and insulated protective box housing the battery, GNSS receiver, and datalogger. Retrieved shortly before the ice they stood upon became unsafe for operations, these stations provide data on the ice dynamics in the months preceding the summer breakout, as well as the end of the breakout of the multi-year fast ice. We calculated station velocities from hourly positions, and used these station velocity data as ground-reference for an InSAR-based method of calculating a 2-dimensional horizontal vector field describing ice motion near Hut Point during early November 2024. We then used this velocity field to calculate its divergence and the principal strain rates for the ice in the area.

The deployment sites for these stations were chosen to cover as well as possible the different ice types in the area, to study their dynamical behaviors and interactions. Thus, we placed Station 1 on the first-year fast ice (specifically, an area that had formed in August), Station 2 on the multi-year fast ice, and Station 3 on the MIS, in order to examine the behavior of these three ice masses shortly before and during part of the sea ice breakout and subsequent MIS calving. Each station's location and average horizontal motion are shown in Fig. 2; a more detailed view of station movement and dates of operation is shown in Fig. 3b.

Due to technical issues – probably solar power problems – some station data were lost. Station 1 functioned intermittently on the days between deployment on 21 October and 17 November, when it began to operate continuously from 17 to 27 November. The cause of this malfunction remains unknown, pending examination and testing of the hardware. Stations 1 and 3 both ceased to consistently function prior to their retrieval; Station 1 approximately seven days prior, and Station 3 approximately eight weeks prior. The Scott Base science technicians who retrieved the stations identified the proximate cause of failure as insufficient power (Dempster, 2024, 2025). A replacement battery was installed in Station 3 on 01 February, allowing approximately one additional week of data collection.

We make use of the GNSS station data in three ways (c.f. Sect. 3.4):

- To gain information on temporal variability in horizontal displacement.
- To account for differential vertical displacement over the study area, in combination with the CATS2008 tide model (an update to the model described by Padman et al., 2002).
- As ground-reference for calibrating the vector field we calculated via InSAR.

https://doi.org/10.5194/egusphere-2025-6300
Preprint. Discussion started: 6 March 2026

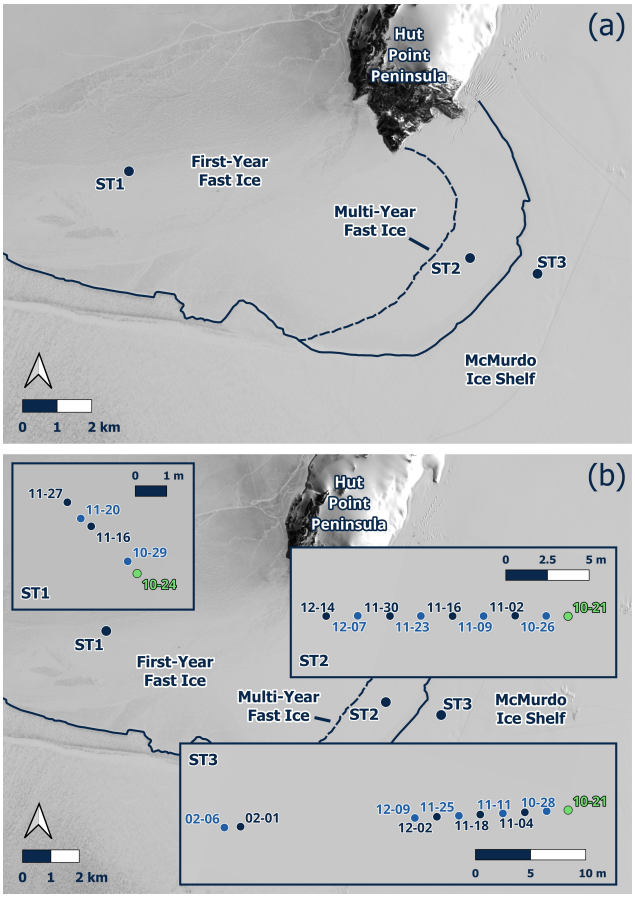

Figure 3. Locations of GNSS stations. Insets show movement during spring 2024 deployment. Full days of operation: Station 1: 29 October, 17 to 27 November; Station 2: 22 October to 13 December; Station 3: 22 October to 08 December, 02 to 06 February. The solid dark line shows the MIS front position; the dashed line represents the multi-year fast ice–first-year fast ice interface. (Background: Landsat panchromatic band, 30 October 2024 (EROS, 2020c).)

3.2 TerraSAR-X data

Our primary remote sensing products are Synthetic Aperture Radar (SAR) TerraSAR-X stripmap images in HH polarization from the German Aerospace Agency (DLR; Breit et al., 2010). Interferograms of the study area calculated from TSX products were used to calculate displacement in the sensor's look direction with a precision of a fraction of the wavelength used by the sensor (Rott, 2009), in our case, a wavelength of ∼3.1 cm.

For our study area, the the ascending- and descending-pass acquisition times are only 3.12 hours apart, so that the 11-day repeat-pass periods overlap by 98.8%. We used ascending-path and descending-path interferometric pairs from TSX which cover the study area, with acquisitions on 19 September, 30 September, 02 November, and 13 November, 2024; ascending path acquisitions at 11:33:08 UTC, and descending path acquisitions at 14:40:18 UTC.

https://doi.org/10.5194/egusphere-2025-6300
Preprint. Discussion started: 6 March 2026

3.3 Landsat data

For identifying the historical extent of the MIS and describing the progression of the summer 2025 sea ice breakout and iceberg calving, we used optical remote sensing products from the NASA/USGS Landsat program (EROS, 2020a, b, c). Almost every day, Landsat produces at least one scene that covers our study area, with 15m resolution for the panchromatic band and 30m resolution for other optical bands (Barsi et al., 2014). Despite the study area being obscured by clouds on some days, Landsat gave us sufficient spatial and temporal resolution to identify the timing of breakout progression and calving events to within a period of no more than a few days, in most cases. For this we used the panchromatic products, and applied contrast stretching to make visual identification of ice boundaries easier.

3.4 Horizontal velocity fields derived from InSAR

Interferometry allows us to use a pair of SAR scenes to calculate the net displacement – in the look direction – that occurred between the acquisitions. With two such component vector fields, calculated from two interferometric pairs acquired from different look angles, and applying the simplifying approximation of horizontal motion, we can calculate a complete 2D velocity field. This concept – with an assumption that ice motion was aligned along the surface – has been applied to glaciers to estimate 3D velocity fields, (e.g. Joughin, 1998). However, as far as we know, this method has not yet been applied to fast ice.

Each interferogram was processed to 15 m resolution. An an adaptive fringe filter was applied, followed by phase unwrapping using a minimum cost flow phase unwrapper algorithm. Each unwrapped interferogram was then used as input to calculate the net displacement during the interval between images, in the look direction projected onto the surface, giving us two component velocity fields.

For the repeat-pass intervals of 19 to 30 September 2024 and 02 to 13 November 2024, we calculated interferograms for ascending- and descending-path TSX image pairs, shown in Fig. 4. The perpendicular baselines for the ascending-path pair and for the descending-path pair ares 62 m (look angle $\sim 39°$) and 31 m (look angle $\sim 35°$), respectively, corresponding to a height ambiguity of about 104 m and 180 m, respectively (Rott, 2009); therefore, we can safely assume a flat surface for both ice shelf and sea ice for the area of our analysis. Comparing the fringe patterns found for our two InSAR intervals informed us about changes in morphology and behavior during the 44 days between the midpoints of the intervals.

Since the November pair of interferograms had higher coherence, we selected that pair for our velocity field and subsequent calculations. The high coherence in our areas of interest indicates that net surface ablation was negligible during the InSAR interval, which is important to justifying part of our interpretation (Sect. 5.2).

We calculated a horizontal free-surface velocity field, relying on the assumption that the displacement detected in the interferograms was dominated by horizontal motion. This assumption is valid if and only if the vertical displacement that occurred between the SAR acquisitions was near-constant in space across the study area, which we were able to check using our GNSS station data, as well as with the CATS2008 tide model (an update to the model described by Padman et al., 2002). For our three GNSS stations, we calculated pairwise linear regressions of the timeseries for change in height. We also compared the

https://doi.org/10.5194/egusphere-2025-6300
Preprint. Discussion started: 6 March 2026

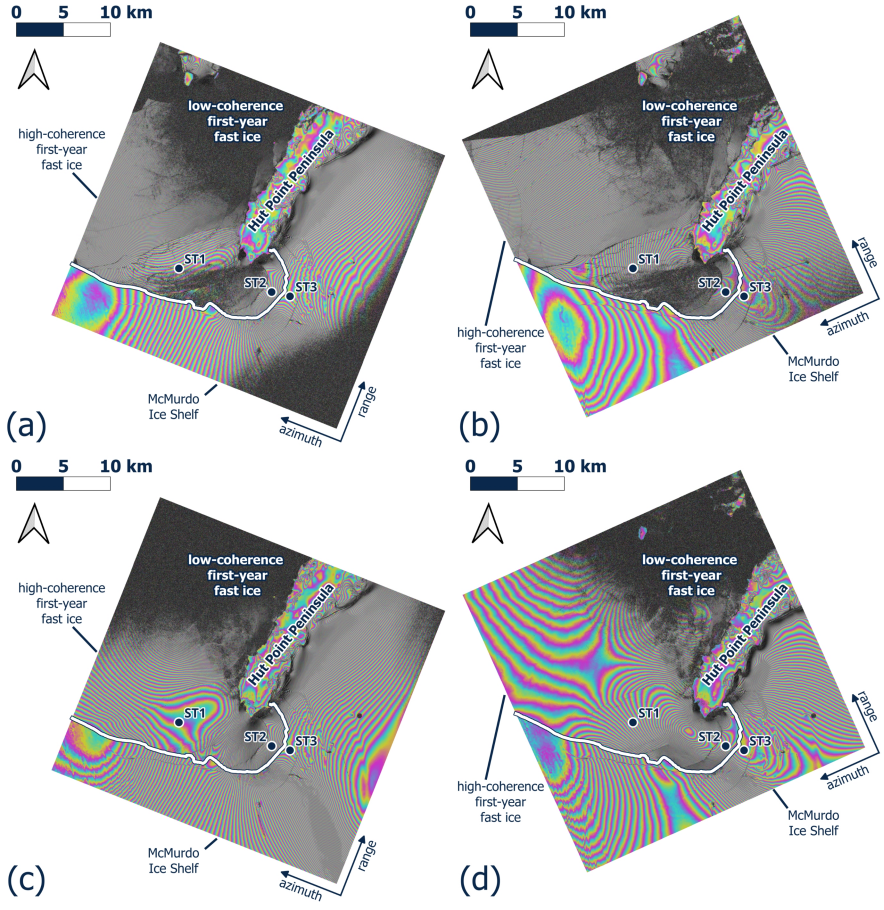

Figure 4. TSX interferograms. **a**: 19 to 30 September 2024, ascending path; **b**: 19 to 30 September 2024, descending path; **c**: 02 to 13 November 2024, ascending path; **d**: 02 to 13 November 2024, descending path. In every panel, the solid white line marks the approximate position of the MIS front. For each acquisition day, ascending path acquisition times were 11:33:08 UTC, and descending path acquisition times were 14:40:18 UTC.

station height-difference timeseries with the tide height measured at Scott Base (LINZ, 2024). We found strong correlations ($R^2 \geq 0.964$) with slopes near 1 (off by at most 0.033) and intercepts near 0 m (off by at most 0.020 m). Additionally, we used the CATS2008 model (an update to the model described by Padman et al., 2002) to calculate that the difference in tide height from one side of McMurdo Sound to the other would contribute at most a single fringe to our interferograms. Based on these calculations, we concluded that uniform tides were the dominant factor in vertical displacement of the ice surface in the study area, and that said vertical displacement was spatially consistent enough that we could consider its contribution to our interferograms to be negligible. A notable exception is the MIS grounding zone along the coast Hut Point Peninsula, where tidal flexure does cause tidal fringes (Rack et al., 2017); this area was excluded.

https://doi.org/10.5194/egusphere-2025-6300
Preprint. Discussion started: 6 March 2026

Table 1. Station velocities used for calibrating the InSAR-derived velocity field subsets, calculated in Universal Transverse Mercator projection. Station 1 calibration velocity calculated from 29 October 00:00 UTC to 28 November 00:00 UTC; Station 2 and 3 calibration velocities calculated from 02 November 11:00 UTC to 13 November 15:00 UTC. Also: station coordinates; ice thickness at Stations 1 and 2 measured 21 October 2024, and estimated at Station 3 from the GNSS sensor height at deployment and by assuming hydrostatic equilibrium.

	Magnitude (cm d^{-1})	Angle (° clockwise from North)	Coordinates (° E, ° S)	Ice thickness (m)
Station 1	9.332	309.0	166.364, 77.866	1.66
Station 2	26.802	263.7	166.787, 77.886	3.69
Station 3	28.434	261.1	166.871, 77.890	41.36

Additionally, we were able to use our GNSS data to verify that the displacement is consistent between acquisition times, and that no abnormal movement was occurring during or between the acquisitions, which allowed us to calculate a full horizontal free-surface velocity field from the ascending- and descending-path images.

To obtain our calibration values, we used the GNSS data from Stations 2 and 3 nearest the first and last of our TSX images used for InSAR (02 November at 11:00 and 13 November at 15:00). We calculated their horizontal displacements in cm d^{-1}, and their angles of motion. Since Station 1 was not operational during the intervals of our InSAR pairs, for it we instead used the difference between its position at the start of its first full day of operation, and the end of its last full day of operation, to calculate its average horizontal displacement in cm d^{-1} and average angle of motion. These values are given in Table 1.

For any pixel in the area for which the ascending- and descending-path interferograms overlap, let $\boldsymbol{u}_{fs,h} = (u_{fs}, v_{fs})$ be the complete 2D horizontal free-surface velocity between the SAR acquisitions, and let $\boldsymbol{a}$ and $\boldsymbol{d}$ be the across-track velocities calculated from the ascending- and descending-path interferograms respectively. From the $\boldsymbol{a}$ and $\boldsymbol{d}$ component fields, we used the fact that $\boldsymbol{a} = proj_{\boldsymbol{a}}(\boldsymbol{u}_{fs,h})$ and $\boldsymbol{d} = proj_{\boldsymbol{d}}(\boldsymbol{u}_{fs,h})$ to derive equations for the components of $\boldsymbol{u}_{fs,h}$ in terms of the components of $\boldsymbol{a}$ and $\boldsymbol{d}$, and calculated $\boldsymbol{u}_{fs,h}$ using a Python script; a full description of this calculation is given in Appendix A.

Our study area contains three distinct zones with boundaries marked by phase discontinuities in the interferograms. Therefore, in order to calibrate the velocity field to the GNSS station data, we separated the field into three simply connected subsets: the first-year fast ice, the multi-year fast ice, and the MIS (containing Station 1, 2, and 3, respectively). We then projected the velocities measured by the GNSS stations onto $\hat{\boldsymbol{a}}$ and $\hat{\boldsymbol{d}}$. For each station location, the difference between the station velocity components and the velocity component fields from InSAR gave correction values for $\boldsymbol{a}$ and $\boldsymbol{d}$ for each subset. We applied each correction value to every point in its subset, calculated u_{fs} and v_{fs} for each, and combined the subsets into a complete vector field.

3.5 Divergence field, and principal strain rates

We applied a shallow-ice approximation – that is, that the vertical velocity profiles of the ice masses are approximately constant – to allow us to take the divergence of the horizontal free-surface velocity field $\mathrm{div}(\boldsymbol{u}_{fs,h})$ as an indication of where the ice was being forced into a smaller horizontal area or expanding into a larger horizontal area. The full justification for this interpretation

https://doi.org/10.5194/egusphere-2025-6300
Preprint. Discussion started: 6 March 2026

is given in Appendix B. To calculate $\mathrm{div}(\boldsymbol{u}_{fs,h}) = \frac{\partial u_{fs}}{\partial x} + \frac{\partial v_{fs}}{\partial y}$, we used a multivariate finite-difference approximation, where our pixel size is 15 m × 15 m, so that $\Delta x = \Delta y = 15$ m.

The shallow-ice approximation also enabled us to use $\boldsymbol{u}_{fs,h}$ to calculate the principal strain rates, as in Harper et al. (1998) and Nye (1959): the magnitudes of the least tensile horizontal axis $\dot{\varepsilon}_1$ and most tensile horizontal axis $\dot{\varepsilon}_3$ are given by

$$\dot{\varepsilon}_1 = \frac{1}{2}\left(\dot{\varepsilon}_x + \dot{\varepsilon}_y\right) - \left(\frac{1}{4}\left(\dot{\varepsilon}_x - \dot{\varepsilon}_y\right)^2 + \dot{\varepsilon}_{xy}^2\right)^{\frac{1}{2}} \tag{1}$$

$$\dot{\varepsilon}_3 = \frac{1}{2}\left(\dot{\varepsilon}_x + \dot{\varepsilon}_y\right) + \left(\frac{1}{4}\left(\dot{\varepsilon}_x - \dot{\varepsilon}_y\right)^2 + \dot{\varepsilon}_{xy}^2\right)^{\frac{1}{2}} \tag{2}$$

where

$$\dot{\varepsilon}_x = \frac{\partial u_{fs}}{\partial x} \tag{3}$$

$$\dot{\varepsilon}_{xy} = \dot{\varepsilon}_{yx} = \frac{1}{2}\left(\frac{\partial u_{fs}}{\partial y} + \frac{\partial v_{fs}}{\partial x}\right) \tag{4}$$

$$\dot{\varepsilon}_y = \frac{\partial v_{fs}}{\partial y} \tag{5}$$

are the strain rates. Taking the y-axis to be northward and taking Φ to be the angle between the y-axis and $\dot{\varepsilon}_1$ for $\dot{\varepsilon}_x > \dot{\varepsilon}_y$, and between the y-axis and $\dot{\varepsilon}_3$ for $\dot{\varepsilon}_x < \dot{\varepsilon}_y$ (Nye, 1959):

$$\Phi = \frac{1}{2}\arctan\left(\frac{2\dot{\varepsilon}_{xy}}{\dot{\varepsilon}_x - \dot{\varepsilon}_y}\right), \Phi \in \left(-\frac{\pi}{4}, \frac{\pi}{4}\right) \tag{6}$$

To calculate strain rates, we again used a multivariate finite-difference approximation, with $\Delta x = \Delta y = 15$ m.

4 Results

In our late-September (Fig. 4, panels a and b) and early-November (Fig. 4, panels c and d) interferograms, both intervals show similar fringe patterns over most of the MIS and the multi-year fast ice, indicating that these areas each have similar behavior during the two intervals. Compared to the late-September interval, the early-November interval shows a denser fringe pattern over the southern MIS, possibly indicating an acceleration. The first-year fast ice is one of the few areas with a significant change in fringe pattern between intervals: in the late-September interferogram there is a discontinuity present at the boundary between older and younger first-year fast ice, which is not present in the early-November interferograms. In the late-September interferograms, part of the first-year fast ice near the end of Hut Point Peninsula – which had formed between March and May 2024 – had low coherence, and by early November coherence in the area was high. Most of the first-year fast ice that did have high coherence in the late-September interval had undergone by the early-November interval a change in fringe pattern and reduced fringe density, and a discontinuity present in the late-September interferograms was absent in the early-November interferograms. These findings are discussed further in Sect. 5.1.

Figure 5 shows $\boldsymbol{u}_{fs,h}$ and $\mathrm{div}(\boldsymbol{u}_{fs,h})$, with locations of GNSS stations marked. Their features are noted in this section and their significance is discussed in Sect. 5.2.

https://doi.org/10.5194/egusphere-2025-6300
Preprint. Discussion started: 6 March 2026

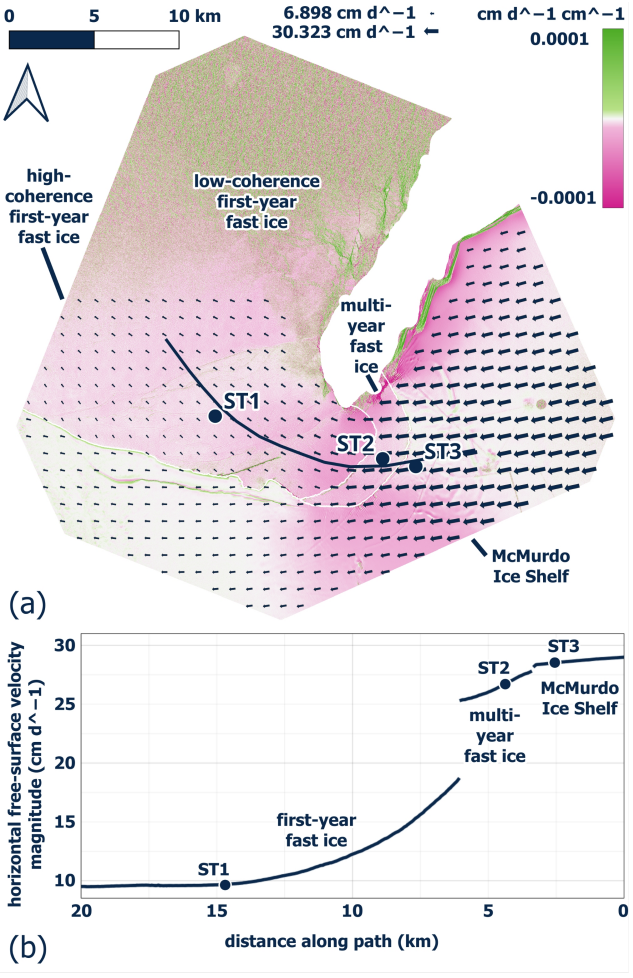

Figure 5. a: Horizontal free-surface velocity field $\boldsymbol{u}_{fs,h}$ (dark blue arrows), and $\mathrm{div}\,(\boldsymbol{u}_{fs,h})$ (green: $\mathrm{div}\,(\boldsymbol{u}_{fs,h}) > 0$ and $w_{fs} < 0$; pink: $\mathrm{div}\,(\boldsymbol{u}_{fs,h}) < 0$ and $w_{fs} > 0$), 02 to 13 November; $||\boldsymbol{u}_{fs,h}||$ values and vector angles are averages within 500 m radii of each grid point, with a grid spacing of 1 km. Subset boundaries are visible as white gaps. The minimum and maximum values shown for $||\boldsymbol{u}_{fs,h}||$ are 6.898 cm d^{-1}, and 30.323 cm d^{-1}, respectively. Where our interferograms had poor coherence and in the tidal flexure zone along the eastern coast of Hut Point Peninsula, our calculated values are not physically meaningful, and $\boldsymbol{u}_{fs,h}$ is not plotted in these areas. Dark blue curve shows the path used for panel **b**: Profile of $||\boldsymbol{u}_{fs,h}||$ along a path passing near the GNSS stations.

In a narrow band east of Hut Point Peninsula (visible in Fig. 5a as stripes of high-magnitude divergence), the MIS experiences large deformation as it flows into Ross Island, and also is subjected to tidal flexure, and interferometry does not give physically meaningful results in this area; it is therefore excluded from our analysis. Likewise, a large northern area of the first-year fast ice had very low coherence in our interferograms, and is omitted from our analysis.

At the interface between the first-year fast ice and the southern MIS, both showed small velocities in respective north-of-westward and westward directions. The first-year fast ice near its interface with the multi-year fast ice had higher velocity and

https://doi.org/10.5194/egusphere-2025-6300
Preprint. Discussion started: 6 March 2026

a slightly north-of-westward direction, compared to the first-year fast ice only a few kilometers from the interface with the multi-year fast ice, which had lower velocity and a more north-of-westward direction.

The magnitude and direction of the multi-year fast ice velocity were more similar to those of the adjoining MIS to the east than to the first-year fast ice, though some deceleration was evident in the area.

In most of the area included in our velocity field, the MIS direction of motion was slightly south-of-west. The MIS had higher velocities to the east and south-east of Hut Point Peninsula, visible in Fig. 5 in an area of very low-magnitude divergence. The southern MIS showed lower velocity and a gradual clockwise change in direction, such that toward the western edge of the field, movement was very slightly north-of-west.

The portion of the southern MIS included in our calculations showed a large area with no clear convergence or divergence, and an area to the west that was dominated by weak divergence.

For both first-year and multi-year fast ice, $\mathrm{div}(\boldsymbol{u}_{fs,h})$ was dominated by convergence. The MIS showed zones of strong convergence, and and with no clear convergence or divergence, as well as an area of weak divergence.

East of Station 3, the MIS had a large area of near-constant velocity and no clear convergence or divergence, suggesting that little deformation was occurring there. Where the edge of this zone meets the adjoining multi-year fast ice, the direction of motion of the MIS was almost directly into the fast ice, inducing convergence in the multi-year fast ice.

To the south of Station 3, we found a transition zone in the MIS, where its movement decelerated and where strong convergence occurred. Where this transition zone meets the multi-year fast ice, the divergence field showed a wave-like pattern of compression.

The $\mathrm{div}(\boldsymbol{u}_{fs,h})$ field also showed several discontinuities, including at the boundaries between different ages of first-year fast ice, and at the location of a large rift in the southern MIS. These are discussed further in Sect. 5.2.

We also calculated the principal strain rates (shown in Fig. 6; discussed further in Sect. 5.2), which indicated that in the large areas of low-magnitude $\mathrm{div}(\boldsymbol{u}_{fs,h})$ to the east of Station 3 and covering the southern MIS, the principal strain rates were small, further suggesting that these areas were behaving as solid masses with little deformation. Similarly, compression ($\dot{\varepsilon}_1 > \dot{\varepsilon}_3$) was dominant in the same areas where the $\mathrm{div}(\boldsymbol{u}_{fs,h})$ field showed convergence and where $\boldsymbol{u}_{fs,h}$ was observed to be decelerating: most strongly in the first-year fast ice near its interface with the multi-year fast ice, as well as in the multi-year fast ice itself and in the transition zone between the southern MIS and the MIS on the east side of the study area.

5 Discussion

For our analysis, we selected a combination of ascending- and descending-path interferograms with 98.8% temporal overlap, which allowed us to produce a precise ice deformation field for the period of 02 to 13 November 2024 which covered out areas of interest. The deformation field was calibrated with co-incident GNSS measurements installed at all major ice types. We chose a second interferogram acquired 44 days earlier showing an overall high phase coherence, allowing a qualitative comparison of the changing fringe pattern. Comparison with our GNSS measurements and the CATS2008 tide model (an update to the model described by Padman et al., 2002) strongly suggests that the fringe pattern seen in the interferograms is

https://doi.org/10.5194/egusphere-2025-6300
Preprint. Discussion started: 6 March 2026

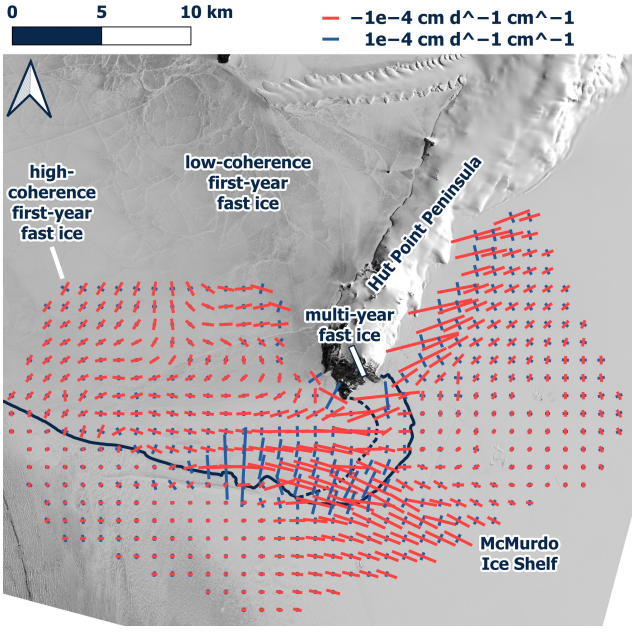

Figure 6. Principal strain rate fields (red: $\dot{\varepsilon}_1$; blue: $\dot{\varepsilon}_3$) calculated from $\boldsymbol{u}_{fs,h}$; values plotted are averages within 500 m radii of each grid point, with a grid spacing of 1 km. The solid dark line shows the MIS front position; the dashed line represents the multi-year fast ice–first-year fast ice interface. Where our interferograms had poor coherence and in the tidal flexure zone along the eastern coast of Hut Point Peninsula, our calculated values are not physically meaningful, and principal strain rates are not plotted in these areas. (Background: Landsat panchromatic band, 30 October 2024 (EROS, 2020c).)

primarily caused by horizontal motion. Apart from the tidal flexure zones, which have been excluded from our analysis, we can assume that less than one fringe is caused by a differential vertical displacement across the study area. Furthermore, most of the MIS and most of the multi-year fast ice showed a similar fringe pattern for both acquisition intervals, which indicates that potentially changing tides did not significantly influence the fringe pattern. Altogether, this enables or significantly simplifies our interpretations.

5.1 Interferograms

Most of the MIS and the multi-year fast ice show similar fringe patterns for both intervals. These similarities indicate that these areas have similar behavior during the two intervals. A small-yet-noticeable difference is that the fringe patterns of the southern MIS are denser in the early-November interferograms, compared to the late-September interferograms, possibly indicating an increase in movement. One of the few areas with a significant change in fringe pattern between intervals is found in the first-year fast ice. In the September interferograms (Fig. 4, panels a and b), the first-year fast ice shows a discontinuity at the boundary between older and younger first-year fast ice; this discontinuity is not present in the November interferograms (Fig. 4, panels c and d), indicating that the different ages of ice became strongly coupled in the interim. In winter of 2024, the

https://doi.org/10.5194/egusphere-2025-6300
Preprint. Discussion started: 6 March 2026

sea ice north of the MIS was frequently blown out. Fast ice at the site of Station 1 only became established around mid-August, and had grown to a thickness of 1.66 m as of 21 October. Such instances of late fast ice consolidation are associated with increased ice tongue velocity (Gomez-Fell et al., 2022) and increased ice shelf calving (Massom et al., 2018), though in our case MIS calving during this period was very minor, possibly due to the presence of the multi-year fast ice covering the part of the front where most calving tends to occur, similar to the observations of Miles et al. (2017) in Porpoise Bay. The fast ice about 3 km north of Station 1 is approximately 3 weeks younger and shows about twice as many fringes in September compared to November, when the boundary between the ages of ice almost completely disappears from our interferograms.

In contrast, part of the first-year fast ice near the end of Hut Point Peninsula – which had formed between March and May 2024 – had low coherence for the late-September interval, and high coherence for the early-November interval; for most of the first-year fast ice that had high coherence in the late-September interval, the fringe pattern changed and fringe density was reduced in the early-November interval, and a discontinuity in the fringe pattern in the late-September interferograms was no longer present in the early-November interferograms. Richter et al. (2024) found that typical monthly average fast ice thickness values observed in McMurdo Sound during this time of year are 164 ± 20 cm in August and increase to 219 ± 26 cm in November. Due to the 2024 fast ice having established late, its thickness at the site of Station 1 on 21 October was still only 1.66 m. The changes we observe between our September and November fringe patterns suggest that despite its late establishment, the growth rates during these months (0.7 ± 0.1 cm d^{-1} in October (Richter et al., 2023)), were sufficient for the first-year fast ice to become stable between the two intervals.

Continuity (or lack thereof) of fringe patterns at the interfaces between ice masses indicates whether they are strongly coupled (Dammann et al., 2016). The interface between the first-year fast ice and the southern MIS was visible in the interferograms as a near-complete discontinuity in the fringe patterns on either side. The exception was the November descending-path interferogram, in which part of the southern MIS front in the west side of the scene showed a fringe pattern that did continue across the front and onto the first-year fast ice. This suggests that the dynamical interaction between the first-year fast ice and the MIS front was weaker than at the other interfaces between ice-forms. Meanwhile, in both ascending-path and the November descending-path interferograms, the fringes on either side of the MIS–multi-year fast ice interface are closely aligned, suggesting that the multi-year fast ice was firmly attached to the MIS and that their dynamics were strongly linked. Similarly, the multi-year fast ice and first-year fast ice exhibited strong coupling.

5.2 Velocity field, divergence of velocity, and principal strain rates

Very high phase coherence enabled successful regional phase unwrapping and the calculation of a velocity field of the fast ice–ice shelf system, which was then calibrated with the GNSS station measurements. The ice velocity profile along an approximate flow line from the MIS ice front to the September fast ice, passing within 1 km of each GNSS station, shows a clear deceleration in the first 15 km. This deceleration indicates that Hut Point Peninsula to the north and the western MIS stabilize the ice shelf front in this area. Pressure ridges in the most southern part of the ice shelf front and near the coast of Hut Point Peninsula are a direct result of this configuration. The velocity profile shows discontinuities between ice shelf, multi-year ice, and first-year ice, which is where sharp Interferometric phase transitions or discontinuities required a separation of regions for the purpose

https://doi.org/10.5194/egusphere-2025-6300
Preprint. Discussion started: 6 March 2026

of successful phase unwrapping and velocity calibration. The discontinuity between the August and September fast ice had disappeared by November, which allowed successful phase unwrapping even for large parts of the September fast ice, where the velocity becomes nearly constant (around km 17.5 in Fig. 5b). In general, the high fringe sequence on the fast ice in all interferograms is a result of the deceleration of the thinner ice rather than acceleration.

We inferred from conservation of momentum that a decelerating flow implies an adverse force, while an accelerating flow implies the opposite. The velocities of the southern MIS and the first-year ice near their interface suggested that the southern MIS was applying a primarily westward forcing to the first-year fast ice, and was not applying any northward forcing. The sudden deceleration and change in direction of movement seen in the first-year fast ice as distance increases from the multi-year fast ice suggests that at their interface, the movement of the multi-year fast ice was applying a forcing to the first-year fast ice, and that their motion was strongly linked, but that this energy of motion was being partially absorbed or dispersed by the first-year fast ice.

The stabilizing effect of fast ice on ice shelf fronts (Christie et al., 2022; Gomez-Fell et al., 2022; Massom et al., 2018; Miles et al., 2017) implies strong coupling at their interface. In our case, the similar velocities of the multi-year fast ice and the adjoining MIS indicated a strong coupling between them, and suggested that the forcing the MIS applied to the multi-year ice at their interface was almost fully propagated and applied in turn to the first-year fast ice.

We took $\mathrm{div}(\boldsymbol{u}_{fs,h})$ (shown in Fig. 5) as an indication of where the ice was being forced into a smaller horizontal area or expanding into a larger horizontal area. The coherence of our interferograms in the areas of interest indicates that net surface ablation was negligible during the InSAR interval, and the presence of the sub-ice platelet layer (e.g. Robinson et al., 2010; Smith et al., 2001) precludes melting from below. Thus from the continuity equation, mass conservation, and the kinematic boundary condition, we concluded that $\mathrm{div}(\boldsymbol{u}_{fs,h})$ also indicated where the ice was undergoing compression and an increase in free-surface height, and where tension and decrease in free-surface height were occurring, possibly indicating thickening and thinning, respectively. Detailed justification is given in Appendix B.

Directly east of Hut Point Peninsula, the MIS was subjected to horizontal compression as it flowed into and around the Peninsula, but the MIS did not accelerate in the process, which implies that it instead deformed. While both the multi-year and first-year fast ice were dominated by convergence, the first-year ice near their interface had stronger convergence then either the first-year ice beyond it or multi-year fast ice. In the same few kilometers in which the velocity field showed large deceleration, the divergence field indicates strong horizontal compression occurred in response to the forcing applied by the multi-year fast ice.

Our $\mathrm{div}(\boldsymbol{u}_{fs,h})$ field showed a few additional noteworthy features.

Near the southern MIS edge, southeast of Station 1, the dominantly convergent first-year fast ice was interrupted by a line of strong convergence and noise. This line was a part of the boundary between a region of first-year fast ice formed in the preceding March, and a region formed in May. Similarly, though more subtly, north of Station 1 was a visible boundary between the first-year fast ice formed in August, and later fast ice. Other, similar-looking lines across the fast ice did not align with areas of different age; we hypothesize that these indicate the presence of large pressure ridges.

https://doi.org/10.5194/egusphere-2025-6300
Preprint. Discussion started: 6 March 2026

The southern MIS front showed a thin band of strong divergence, suggesting the edge might be in the process of calving. However, calving along this part of the MIS front was very minor in the 2025 summer, making the significance of this band of divergence less clear.

A large rift near the southern MIS front (visible in the satellite record for at least a dozen years) appeared as sharp arc of divergence on the south side of the rift and convergence on the north side. On the eastern end of the rift, calving in recent years has brought the MIS front near the rift. Meanwhile, the rift has extended westward. Since the stabilizing of the calving front by the fast ice along this part of the front was weak, it is likely that calving along this rift is imminent, especially if the eastern end of the rift continues to extend toward the ice shelf front. While most of the southern MIS had low principal strain rate values, larger values were found close to the this rift, a sign that the rift will continue to grow. Crevasses primarily form or expand in the direction normal to the most tensile strain rate ε_3 (Han and Lee, 2018), and so the values of our principal strain rate field near the rift (c.f. Fig. 6) suggest it is likely to continue extending to the east or east or northeast and west or southwest.

In contrast to what $\boldsymbol{u}_{fs,h}$ and $\mathrm{div}(\boldsymbol{u}_{fs,h})$ showed about the behavior of the multi-year fast ice, the principal strain rates reveal a way in which the multi-year fast ice behaved more similarly to the first-year fast ice than to the MIS. The multi-year fast ice had larger compressive and extensive strain rates than the MIS pressing against it, despite $\mathrm{div}(\boldsymbol{u}_{fs,h})$ remaining small over most of the multi-year fast ice. The compressive strain is larger yet in the part of the first-year fast ice near the multi-year fast ice, indicating yet more compressive deformation as force is absorbed. Han and Lee (2018) found that fast ice had smaller strain rates as it thickened, which suggests that under similar forces thicker ice is expected to have smaller strain rates than thinner ice; in our scenario, this is the case despite the thicker fast ice being subjected to stronger forcing.

5.3 Ice shelf calving and fast ice breakout

The existence of fast ice in the Hut Point Peninsula embayment suggests a stabilizing influence on the MIS front, similar to the findings of studies conducted in other regions (e.g. Christie et al., 2022; Massom et al., 2018; Miles et al., 2017). In recent years, an increase in fast ice breakout during winter has been observed (e.g. Leonard et al., 2021). Our analysis shows that the MIS ice front has undergone large net retreat since the early 1960s, and in summer 2025 experienced net retreat to a minimum beyond any found in the Landsat 4–9 record (c.f. Fig. 1). Miles et al. (2017) found that in Porpoise Bay, a similar breakout of multi-year fast ice was likely connected to the calving events that shortly followed. In our case, beginning less than a day after the fast ice breakout was complete, iceberg calving occurred in February 2025 along the ice shelf front south of Hut Point Peninsula – including the vicinity of Station 3 (c.f. Fig. 2). When Station 3 was deployed (21 October 2024), it was located $\sim$700 m from the MIS front; once the calving was complete (c. 11 March 2025), the new front position was $\sim$20 m from where Station 3 had been. From the surface elevation at Station 3 (5.15 m above water level, 21 October 2024) and the assumption of hydrostatic equilibrium, we estimated the ice shelf thickness near the front to be 41.36 m, only ~ 11 times the fast ice thickness at Station 2 (c.f. Table 1), which suggests there is likely a direct dynamical influence beyond the protection from ocean swell or delay of iceberg calving. Our observed strain and velocity fields indicate a back-pressure in this area, and the findings of Gomez-Fell et al. (2022) suggest an acceleration of the MIS post-breakout is a possibility, but other than the observed calving we do not have observational data which show a change in ice shelf dynamics immediately after breakout. However, precise

https://doi.org/10.5194/egusphere-2025-6300
Preprint. Discussion started: 6 March 2026

observations such as those presented here are a basis which will allow further study of the interaction between fast ice and ice shelf in this region and beyond.

6 Conclusions

Our velocity field, divergence of velocity, and principal strain rates, taken together, clearly showed the fast ice in the embayment decelerating and compressing in response to forcing from the MIS to the east. This implies an equal force was being applied to the MIS front by the fast ice. Since our $\mathrm{div}(\boldsymbol{u}_{fs,h})$ and principal strain rate fields showed this part of the MIS was not significantly deforming, this forcing being applied to the MIS front must have had a stabilizing effect rather than inducing significant deformation. Given the suddenness, speed, and quantity of calving from this portion of the MIS front following the fast ice breakout (c.f. Fig. 2), the stabilizing effect appears to have been large.

However, the southern MIS front behaved rather differently. It appeared to have only weak coupling and dynamical interaction with the adjoining fast ice, and therefore received very little stabilizing effect from the fast ice. Despite this, the southern MIS front underwent only minor calving during summer 2025, meaning that, at least this year, it did not require a forcing from the fast ice to remain stable. As the large rift near the southern MIS front continues to grow, in future years, either the front will begin applying a stronger forcing to the adjoining fast ice – and experience a stabilizing effect similar to the MIS front southeast of Hut Point, or coupling between the southern MIS front and the fast ice will continue to be minimal and calving may occur regardless of the presence of fast ice.

The possibility of future changes in the formation, duration, and breakout of fast ice makes this embayment a location of continued interest. Thinner fast ice would less effectively absorb the force placed upon it, resulting in a weaker stabilizing forcing on the MIS front, potentially resulting in the front being less structurally sound when the fast ice breakout occurs, leading to increased calving. Earlier fast ice breakouts would result in a larger fraction of the summer during which the MIS front lacks the stabilizing influence of the fast ice, and our findings imply that this would result in more calving. Additionally, the ice shelf front would be more exposed to solar-heated surface water, which could enhance melting, while the absence of fast ice would leave the front vulnerable to mechanical action from waves and swell.

As the Antarctic cryosphere responds to the warming of ocean and atmosphere, it will be important to better understand the stabilizing effect of fast ice on the MIS front in this embayment, since doing so will allow us to better monitor and predict the evolution of the MIS, ice shelves in general, and the ice sheets they buttress. Using our methodology to compare surface velocity, divergence of velocity, and principal strain rates from before an after a fast ice breakout, we could gain a more complete understanding of the influence of the fast ice. Furthermore, modeling studies of the ice dynamics in this embayment can offer further insight into the fast ice–ice shelf relationship.

Code and data availability. Our McMurdo Soun GNSS data (Price et al., 2025) are available at https://doi.org/10.26021/canterburynz.30768455.v2. The Python scripts used for our calculations are available upon request.

https://doi.org/10.5194/egusphere-2025-6300
Preprint. Discussion started: 6 March 2026

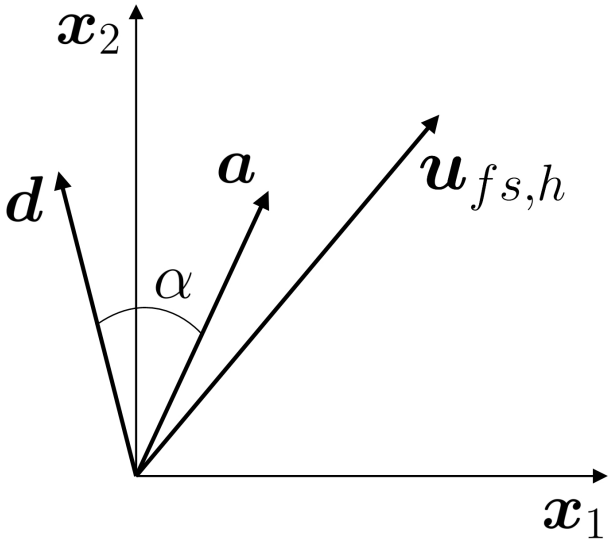

Figure A1. Illustration of vectors for ice surface motion at a given point.

Appendix A: Horizontal velocity field calculation details

For any pixel in the area for which the ascending- and descending-path interferograms overlap, let $\boldsymbol{u}_{fs,h}$ be the complete 2D horizontal free-surface velocity between the SAR acquisitions, let $\boldsymbol{a}$ and $\boldsymbol{d}$ be the across-track velocities calculated from the ascending- and descending-path interferograms respectively, and let α be the angle between $\boldsymbol{a}$ and $\boldsymbol{d}$ (illustrated in Fig. A1).

Then $\boldsymbol{a}$ is the projection of $\boldsymbol{u}_{fs,h}$ onto the ascending-path across-track direction $\hat{\boldsymbol{a}}$, and $\boldsymbol{d}$ is the projection of $\boldsymbol{u}_{fs,h}$ onto the descending-path across-track direction $\hat{\boldsymbol{d}}$. That is

$$\boldsymbol{a} = proj_{\boldsymbol{a}}(\boldsymbol{u}_{fs,h}) = (\boldsymbol{a}\cdot\boldsymbol{u}_{fs,h})\,\hat{\boldsymbol{a}} = \frac{\boldsymbol{a}\cdot\boldsymbol{u}_{fs,h}}{\boldsymbol{a}\cdot\boldsymbol{a}}\boldsymbol{a} \tag{A1}$$

$$\boldsymbol{d} = proj_{\boldsymbol{d}}(\boldsymbol{u}_{fs,h}) = (\boldsymbol{d}\cdot\boldsymbol{u}_{fs,h})\,\hat{\boldsymbol{d}} = \frac{\boldsymbol{d}\cdot\boldsymbol{u}_{fs,h}}{\boldsymbol{d}\cdot\boldsymbol{d}}\boldsymbol{d} \tag{A2}$$

from which we derived the following equations for the eastward (u_{fs}) and northward (v_{fs}) components of $\boldsymbol{u}_{fs,h}$ in terms of the eastward (subscript 1) and northward (subscript 2) components of $\boldsymbol{a}$ and $\boldsymbol{d}$:

$$u_{fs} = \frac{\boldsymbol{d}\cdot\boldsymbol{d} - \frac{d_2}{d_1}\boldsymbol{a}\cdot\boldsymbol{a}}{d_1\left(1 - \frac{d_2}{d_1}\frac{a_1}{a_2}\right)} \tag{A3}$$

$$v_{fs} = \frac{\boldsymbol{a}\cdot\boldsymbol{a} - a_1 u_{fs}}{a_2} \tag{A4}$$

We performed these calculations for each 15 m × 15 m pixel in the overlap of the ascending and descending scenes.

https://doi.org/10.5194/egusphere-2025-6300
Preprint. Discussion started: 6 March 2026

Appendix B: Interpretation of $\mathrm{div}(\boldsymbol{u}_{fs,h})$

To justify our interpretation of $\mathrm{div}(\boldsymbol{u}_{fs,h})$, we begin from the continuity equation for 3D flow:

$$\frac{\partial \rho}{\partial t} + \mathrm{div}\,(\rho \boldsymbol{u}) = 0 \tag{B1}$$

where $\boldsymbol{u} = (u, v, w)$ is the 3D velocity of the fluid. The ice-forms we were concerned with have approximately constant density, which allows us to simplify Eq. (B1) to

$$\mathrm{div}\,(\boldsymbol{u}) = \frac{\partial u}{\partial x} + \frac{\partial v}{\partial y} + \frac{\partial w}{\partial z} = 0 \tag{B2}$$

Since our InSAR calculations gave us the horizontal free surface velocity components u_{fs} and v_{fs}, we required two additional relationships. First, the depth-averaged mass conservation equation states

$$\frac{\partial h}{\partial t} + \mathrm{div}\,(h\boldsymbol{u}_{av}) = 0 \tag{B3}$$

or

$$\frac{\partial h}{\partial t} + h\mathrm{div}\,(\boldsymbol{u}_{av}) + \boldsymbol{u}_{av} \cdot \nabla h = 0 \tag{B4}$$

where $\boldsymbol{u}_{av} = (u_{av}, v_{av})$ is the depth-averaged velocity.

Second, the kinematic boundary condition requires that

$$\frac{\partial h}{\partial t} + u_{fs}\frac{\partial h}{\partial x} + v_{fs}\frac{\partial h}{\partial y} = w_{fs} \tag{B5}$$

which can be rewritten as

$$\frac{\partial h}{\partial t} + \boldsymbol{u}_{fs} \cdot \nabla h = w_{fs} \tag{B6}$$

Under the assumption that horizontal free surface velocity and depth-averaged velocity are proportional – i.e.: $(u_{fs}, v_{fs}) = \alpha \cdot (u_{av}, v_{av})$ for some constant scalar α – we can simplify Eq. (B6) to

$$\frac{\partial h}{\partial t} + \alpha \boldsymbol{u}_{av} \cdot \nabla h = w_{fs} \tag{B7}$$

Then, Eq. (B4) and (B7) give us

$$\frac{\partial h}{\partial t}\left(1 - \frac{1}{\alpha}\right) + h \cdot \mathrm{div}\left(\frac{1}{\alpha}\boldsymbol{u}_{fs}\right) + \frac{w_{fs}}{\alpha} = 0 \tag{B8}$$

For the ice-forms we were concerned with, we could apply a shallow-ice approximation, and assume the free surface velocity is approximately equal to the depth-averaged velocity, so that $\alpha \approx 1$, and thus we approximate Eq. (B8) as

$$\mathrm{div}\,(\boldsymbol{u}_{fs}) + \frac{w_{fs}}{h} = 0 \tag{B9}$$

https://doi.org/10.5194/egusphere-2025-6300
Preprint. Discussion started: 6 March 2026

which allowed us to conclude that $\mathrm{div}(\boldsymbol{u}_{fs,h})$ is related to the vertical free surface velocity scaled by the thickness of the ice, and so convergence and divergence imply respective raising and lowering of the free surface – though without knowing the ice thickness we do not know the magnitude of the change in surface height. Convergence and rising free-surface height is a possible indication of – but does not necessarily imply – the ice thickening; similarly divergence and lowering free-surface height indicates possible ice thinning.

Author contributions. Kallie Bohn, Wolfgang Rack, and Dan Price developed the concept of the study, conceived the fieldwork plan, and conducted the fieldwork. Dan Price led the SAR image acquisition planning and tasking. Mathieu Sellier supported the interpretation of the velocity field and the derived satellite data products. Rodrigo Gomez-Fell and Wolfgang Rack contributed to SAR image processing and interpretation. Kallie Bohn led the manuscript writing. All co-authors supported discussions around data interpretation and manuscript writing and revision.

Competing interests. The authors declare an absence of competing interests.

Acknowledgements. The authors thank Antarctica New Zealand and all summer 2024 Scott Base personnel for making our in situ measurements possible; with special thanks to Alec Dempster, Tom King, and their teams of Scott Base Science Technicians, for their assistance maintaining and retrieving the GNSS stations. We are grateful to Pauline Barras and Adrian Tan for their help deploying the GNSS stations, and to Pauline for conducting ice thickness measurements at the sites of Stations 1 and 2 (included in Table 1), as part of Event K053 (2024). Thanks also to the Event K892 (2024) field team, and especially Greg Leonard, for helping with GNSS station maintenance. We are also grateful to Heather Purdie and Paul Bealing of the University of Canterbury School of Earth and Environment, for their guidance on processing the GNSS data.

Thanks also to Miriam Sterl and Lin Wouters for helping refine the Plain-Language Summary, improving its accessibility and clarity for a broad audience.

Figures 1–6 were made using QGIS 3.40 (2024). Field plots in Fig. 5 and 6 where made in part using the QGIS Point Sampling Tool plugin (https://github.com/borysiasty/pointsamplingtool). Figure A1 made with LibreOffice Draw.

We thank the German Aerospace Center (DLR) for support in the form of TerraSAR-X satellite data under project HYD3673.

The Landsat images used in this study were distributed by the Alaska Satellite Facility.

Geospatial support for this work provided by the Polar Geospatial Center under NSF-OPP awards 1043681, 1559691, and 2129685.

Kallie Bohn was supported by a University of Canterbury Sustainable Development Goals PhD Scholarship.

https://doi.org/10.5194/egusphere-2025-6300
Preprint. Discussion started: 6 March 2026

References

Amante, C. and Eakins, B.W.: ETOPO1 1 Arc-Minute Global Relief Model: Procedures, Data Sources and Analysis, NOAA Technical Memorandum NESDIS NGDC-24 [Data set], National Geophysical Data Center, NOAA, https://doi.org/10.7289/V5C8276M, 2009.

Arndt, J.E., Schenke, H.W., Jakobsson, M., Nitsche, F.O., Buys, G., Goleby, B., Rebesco, M., Bohoyo, F., Hong, J., Black, J., Greku, R., Udintsev, G., Barrios, F., Reynoso-Peralta, W., Taisei, M., and Wigley, R.: The International Bathymetric Chart of the Southern Ocean (IBCSO) Version 1.0—A new bathymetric compilation covering circum-Antarctic waters [data set], Geophys. Res. Lett., 40, 3111–3117, https://doi.org/10.1002/grl.50413, 2013.

Barsi, J.A., Lee, K., Kvaran, G., Markham, B., and Pedelty, J.A.: The Spectral Response of the Landsat-8 Operational Land Imager, Remote Sensing, 6(10), 10232–10251, https://doi.org/10.3390/rs61010232, 2014.

Breit, H., Fritz, T., Balss, U., Lachaise, M., Niedermeier, A., and Vonavka, M.: TerraSAR-X SAR Processing and Products, IEEE Trans. Geosci. Remote Sens., 48(2), 727–740, https://doi.org/10.1109/TGRS.2009.2035497, 2010.

Chen, Z., Montpetit, B., Banks, S., White, L., Behnamian, A., Duffe, J., and Pasher, J.: InSAR monitoring of arctic landfast sea ice deformation using L-band ALOS-2, C-band Radarsat-2 and Sentinel-1, Remote Sensing, 13(22), 4570, https://doi.org/10.3390/rs13224570, 2021.

Christie, F.D.W., Benham, T.J., Batchelor, C.L., Rack, W., Montelli, A., and Dowdeswell, J.A.: Antarctic ice-shelf advance driven by anomalous atmospheric and sea-ice circulation, Nat. Geosci., 15, 356–362, https://doi.org/10.1038/s41561-022-00938-x, 2022.

Dammann, D.O., Eicken, H., Meyer, F.J., and Mahoney, A.R.: Assessing small-scale deformation and stability of landfast sea ice on seasonal timescales through L-band SAR interferometry and inverse modeling, Remote Sens. Environ., 187, 492–504, https://doi.org/10.1016/j.rse.2016.10.032, 2016.

Dammann, D.O., Eicken, H., Mahoney, A.R., Saiet, E., Meyer, F.J., and George, J.C.: Traversing Sea Ice—Linking Surface Roughness and Ice Trafficability Through SAR Polarimetry and Interferometry, IEEE J-STARS, 11(2), 416–433, https://doi.org/10.1109/jstars.2017.2764961, 2017.

Dammann, D.O., Eicken, H., Mahoney, A.R., Meyer, F.J., Freymueller, J.T., and Kaufman, A.M.: Evaluating landfast sea ice stress and fracture in support of operations on sea ice using SAR interferometry, Cold Reg. Sci. Technol., 149, 51–64, https://doi.org/10.1016/j.coldregions.2018.02.001, 2018.

Dammann, D.O., Eriksson, L.E.B., Mahoney, A.R., Eicken, H., and Meyer, F.J.: Mapping pan-Arctic landfast sea ice stability using Sentinel-1 interferometry, The Cryosphere, 13, 557–577, https://doi.org/10.5194/tc-13-557-2019, 2019.

Dempster, A., Scott Base Summer Science Technician. Email to authors, 05 December 2024.

Dempster, A., Scott Base Summer Science Technician. Email to authors, 07 February 2025.

Dierking, W., Lang, O., and Busche, T.: Sea ice local surface topography from single-pass satellite InSAR measurements: a feasibility study, The Cryosphere, 11, 1967–1985, https://doi.org/10.5194/tc-11-1967-2017, 2017.

Dupont, T.K. and Alley, R.B.: Assessment of the importance of ice-shelf buttressing to ice-sheet flow, Geophys. Res. Lett., 32, L04503, https://doi.org/10.1029/2004GL022024, 2005.

Earth Resources Observation and Science (EROS) Center: Landsat 4–5 Thematic Mapper Level-1, Collection 2 [Dataset], U.S. Geological Survey, https://doi.org/10.5066/P918ROHC, 2020.

Earth Resources Observation and Science (EROS) Center: Landsat 7 Enhanced Thematic Mapper Plus Level-1, Collection 2 [Dataset], U.S. Geological Survey, https://doi.org/10.5066/P9TU80IG, 2020.

https://doi.org/10.5194/egusphere-2025-6300
Preprint. Discussion started: 6 March 2026

Earth Resources Observation and Science (EROS) Center: Landsat 8–9 Operational Land Imager / Thermal Infrared Sensor Level-1, Collection 2 [Dataset], U.S. Geological Survey, https://doi.org/10.5066/P975CC9B, 2020.

Fedders, E.R., Mahoney, A.R., Dammann, D.O., Polashenski, C., and Hutchings, J.K.: Two-dimensional thermal and dynamical strain in landfast sea ice from InSAR: results from a new analytical inverse method and field observations, Ann. Glaciol., 1–14, https://doi.org/10.1017/aog.2024.29, 2024.

Fraser, A.D., Massom, R.A., Michael, K.J., Galton-Fenzi, B.K., and Lieser, J.L.: East Antarctic Landfast Sea Ice Distribution and Variability, 2000–08, J. Climate., 25, 1137–1156, https://doi.org/10.1175/JCLI-D-10-05032.1, 2012.

Gomez-Fell, R., Rack, W., Purdie, H., and Marsh, O.: Parker Ice Tongue collapse, Antarctica, triggered by loss of stabilizing land-fast sea ice, Geophys. Res. Lett., 49, e2021GL096156, https://doi.org/10.1029/2021GL096156, 2022.

Gomez-Fell, R., Rack, W., Marsh, O.J., and Purdie, H.: Lateral flexure of Erebus Ice Tongue due to ocean current forcing and fast ice coupling, J. Glaciol., 70, e37, 1–13, https://doi.org/10.1017/jog.2024.21, 2024.

Gow, A.J. and Govoni, J.W.: An 80 year record of retreat of the Koettlitz Ice Tongue, McMurdo Sound, Antarctica, Ann. Glaciol., 20, 237–241, 1994.

Haas, C., Langhorne, P.J., Rack, W., Leonard, G.H., Brett, G.M., Price, D., Beckers, J.F., and Gough, A.J.: Airborne mapping of the sub-ice platelet layer under fast ice in McMurdo Sound, Antarctica, The Cryosphere, 15, 247–264, https://doi.org/10.5194/tc-15-247-2021, 2021.

Han, H. and Lee, H.: Glacial and tidal strain of landfast sea ice in Terra Nova Bay, East Antarctica, observed by interferometric SAR techniques, Remote Sens. Environ., 209, 41–51, https://doi.org/10.1016/j.rse.2018.02.033, 2018.

Harper, J.T., Humphrey, N.F., and Pfeffer, W.T.: Crevasse patterns and the strain-rate tensor: a high-resolution comparison, J. Glacio., 44(146), 68–76, https://doi.org/10.3189/S0022143000002367, 1998.

Jensen, D.A., Nandan, V., Mahoney, A.R., Yackel, J.J., and Resler, L.M.: Landfast sea ice break out patterns in the northern Bering Sea observed from C-band Synthetic Aperture Radar, Int. J. Appl. Earth Obs. Geoinf., 117, 103183, https://doi.org/10.1016/j.jag.2023.103183, 2023.

Joughin, I.R., Kwok, R., and Fahnestock, M.A.: Interferometric estimation of three-dimensional ice-flow using ascending and descending passes, IEEE T. Geosci. Remote., 36(1), 25–37, 1998.

Kim, S., Saenz, B., Scanniello, J., Daly, K., and Ainley, D.: Local climatology of fast ice in McMurdo Sound, Antarctica, Antarct. Sci., 30, 125–142, https://doi.org/10.1017/S0954102017000578, 2018.

Langhorne, P.J., Haas, C., Price, D., Rack, W., Leonard, G.H., Brett, G.M., and Urbini, S.: Fast ice thickness distribution in the western Ross Sea in late spring, J. Geophys. Res. Oceans, 128, e2022JC019459, https://doi.org/10.1029/2022JC019459. 2023.

Land Information New Zealand. Tidegauge data [dataset]. https://sealevel-data.linz.govt.nz/index.html

Leonard, G.H., Langhorne, P.J., Williams, M.J.M., Vennell, R., Purdie, C.R., Dempsey, D.E., Haskell, T.G., and Frew, R.D.: Evolution of supercooling under coastal Antarctic sea ice during winter, Antarct. Sci., 23, 399–409, https://doi.org/10.1017/S0954102011000265, 2011.

Leonard, G.H., Turner, K.E., Richter M.E., Whittaker, M.S., and Smith, I.J.: Brief communication: The anomalous winter 2019 sea-ice conditions in McMurdo Sound, Antarctica, The Cryosphere, 15, 4999–5006, https://doi.org/10.5194/tc-15-4999-2021, 2021.

Li, S., Shapiro, L., Mcnutt, L., and Feffers, A.: Application of Satellite Radar Interferometry to the Detection of Sea Ice Deformation, J. Remote Sens. Soc. Jpn, 16(2), 153–163, https://doi.org/10.11440/rssj1981.16.153, 1996.

Liu, H., Jezek, K.C., Li, B., and Zhao, Z.: Radarsat Antarctic Mapping Project Digital Elevation Model, Version 2, 200m resolution [data set], Boulder, Colorado USA, NASA National Snow and Ice Data Center Distributed Active Archive Center, http://dx.doi.org/10.5067/8JKNEW6BFRVD, 2015.

https://doi.org/10.5194/egusphere-2025-6300
Preprint. Discussion started: 6 March 2026

Mahoney, A.R., Gough, A.J., Langhorne, P.J., Robinson, N.J., Stevens, C.L., Williams, M.M.J., and Haskell, T.G.: The seasonal appearance of ice shelf water in coastal Antarctica and its effect on sea ice growth, J. Geophys. Res.: Oceans, 116, C11032, https://doi.org/10.1029/2011jc007060, 2011.

Mahoney, A.R., Dammann, D.O., Johnson, M.A., Eicken, H., and Meyer F.J.: Measurement and imaging of infragravity waves in sea ice using InSAR, Geophys. Res. Lett., 43, 6383–6392, https://doi.org/10.1002/2016GL069583, 2016.

Massom, R.A., Scambos, T.A., Bennetts, L.G., Reid, P., Squire, V.A., and Stammerjohn, S.E.: Antarctic ice shelf disintegration triggered by sea ice loss and ocean swell, Nature, 558, 383–400, https://doi.org/10.1038/s41586-018-0212-1, 2018.

Matsuoka, K., Skoglund, A., and Roth, G.: Quantarctica [data set], Norwegian Polar Institute, https://doi.org/10.21334/npolar.2018.8516e961, 2018.

Meyer, F.J., Mahoney, A.R, Eicken, H., Denny, C.L., Druckenmiller, H.C., and Hendricks, S.: Mapping arctic landfast ice extent using L-band synthetic aperture radar interferometry, Remote Sens. Environ., 115(12), 3029–3043, https://doi.org/10.1016/j.rse.2011.06.006, 2011.

Miles, B.W.J., Stokes, C.R., and Jamieson, S.S.R.: Simultaneous disintegration of outlet glaciers in Porpoise Bay (Wilkes Land), East Antarctica, driven by sea ice break-up, The Cryosphere, 11, 427–442, https://doi.org/10.5194/tc-11-427-2017, 2017.

Morris, K., Li, S., and Jeffries, M.: Meso-and microscale sea-ice motion in the East Siberian Sea as determined from ERS-I SAR data, J. Glaciol., 45(150), 370–383, https://doi.org/10.3189/S0022143000001878, 1999.

Nye J.F.: A Method of Determining the Strain-Rate Tensor at the Surface of a Glacier, J. Glacio., 3(25), 409–419, https://doi.org/10.3189/S0022143000017093, 1959.

Padman, L., Fricker, H.A., Coleman, R., Howard, S., and Erofeeva, S.: A new tidal model for the Antarctic ice shelves and seas, Ann. Glaciol., 34, 247–254, https://doi.org/10.3189/172756402781817752, 2002.

Price, D., Rack, W., Langhorne, P.J., Haas, C., Leonard, G., and Barnsdale, K.: The sub-ice platelet layer and its influence on freeboard to thickness conversion of Antarctic sea ice, The Cryosphere, 8, 1031–1039, https://doi.org/10.5194/tc-8-1031-2014, 2014.

Price, D., Rack, W., Gomez-Fell, R., Bohn, K., and Sellier, M.: McMurdo Sound GNSS Files 2024/2025. University of Canterbury Data Repository [data set], https://doi.org/10.26021/canterburynz.30768455.v2, 2025.

QGIS Development Team: QGIS Geographic Information System, Open Source Geospatial Foundation Project, http://qgis.osgeo.org, 2024.

Rack, W., King, M.A., Marsh, O.J., Wild, C.T., and Floricioiu, D.: Analysis of ice shelf flexure and its InSAR representation in the grounding zone of the southern McMurdo Ice Shelf, The Cryosphere, 11, 2481–2490, https://doi.org/10.5194/tc-11-2481-2017, 2017.

Rack, W., Price, D., Haas, C., Langhorne, P.J., and Leonard, G.H.: Sea ice thickness in the Western Ross Sea, Geophys. Res. Lett., 48, e2020GL090866, https://doi.org/10.1029/2020GL090866, 2021.

Richter, M.E., Leonard, G.H., Smith, I.J., Langhorne, P.J., Mahoney, A.R., and Parry, M.: Accuracy and precision when deriving sea-ice thickness from thermistor strings: a comparison of methods, J. Glaciol., 69(276), 879–898, https://doi.org/10.1017/jog.2022.108, 2023.

Richter, M.E., Leonard, G.H., Smith, I.J., Langhorne, P.J., and Parry, M.: The interannual variability of Antarctic fast-ice thickness in McMurdo Sound and connections to climate, J. of Geophys. Res.: Oceans, 129, e2023JC020134, https://doi.org/10.1029/2023JC020134, 2024.

Robinson, N.J., Williams, M.J.M., Barrett, P.J., and Pyne, A.R.: Observations of flow and ice-ocean interaction beneath the McMurdo Ice Shelf, Antarctica, J. Geophys. Res., 115, C03025, https://doi.org/10.1029/2008JC005255, 2010.

Rott, H.: Advances in interferometric synthetic aperture radar (InSAR) in earth system science, Prog. Phys. Geo., 33(6), 769–791, https://doi.org/10.1177/0309133309350263, 2009.

https://doi.org/10.5194/egusphere-2025-6300
Preprint. Discussion started: 6 March 2026

Rott, H., Rack, W., Skvarca, P., and De Angelis, H.: Northern Larsen Ice Shelf, Antarctica: further retreat after collapse, Ann. Glaciol., 34, 277–282, https://doi.org/10.3189/172756402781817716, 2017.

Smith, I.J., Langhorne, P.J., Haskell, T.G., Trodahl, H.J., Frew, R., and Vennell, R.: Platelet ice and the land-fast sea ice of McMurdo Sound, Antarctica, Ann. Glaciol., 33, 21–27, https://doi.org/10.3189/172756401781818365, 2001.

Tinto, K.J., Padman, L., Siddoway, C.S., et al.: Ross Ice Shelf response to climate driven by the tectonic imprint on seafloor bathymetry, Nat. Geosci. 12, 441–449, https://doi.org/10.1038/s41561-019-0370-2, 2019.

Van der Sanden, J. and Short, N.: Radar satellites measure ice cover displacements induced by moving vehicles, Cold Reg. Sci. Technol., 133, 56–62, https://doi.org/10.1016/j.coldregions.2016.10.001, 2017.

Wang, Z., Wang, Z., Li, H., Ni, P., and Liu, J.: A Modified Approach of Extracting Landfast Ice Edge Based on Sentinel-1A InSAR Coherence Image in the Gulf of Bothnia, J. Mar. Sci. Eng., 9, 1076, https://doi.org/10.3390/jmse9101076, 2021.

Wuite, J., Rott, H., Hetzenecker, M., Floricioiu, D., De Rydt, J., Gudmundsson, G. H., Nagler, T., and Kern, M.: Evolution of surface velocities and ice discharge of Larsen B outlet glaciers from 1995 to 2013, The Cryosphere, 9, 957–969, https://doi.org/10.5194/tc-9-957-2015, 2015.